Frontiers in Heat and Mass Transfer

Available at www.ThermalFluidsCentral.org

DIRECT SIMULATIONS OF BIPHILIC-SURFACE CONDENSATION: OPTIMIZED SIZE EFFECTS

Zijie Chen[a], Sanat Modak [a], Massoud Kaviany [a,*], Richard Bonner [b]

[a] Department of Mechanical Engineering, University of Michigan, Ann Arbor, MI, 48109, the United States
[b] Advanced Cooling Technologies, Lancaster, PA, 17601, the United States

ABSTRACT

In dropwise condensation on vertical surface, droplets grow at nucleation sites, coalesce and reach the departing diameter. In biphilic surfaces, when the hydrophobic domain is small, the maximum droplet diameter is controlled by the shortest dimension where the droplets merge at the boundary. Through direct numerical simulations this size-effect heat transfer coefficient enhancement is calculated. Then the 1-D biphilic surface is optimized considering the size-dependent hydrophilic domain partial flooding (directly simulated as a liquid rivulet and using the capillary limit), the subcooling (heat flux) and condenser length effects. The predicted performance is in good agreement with the available experiments.

Keywords: *Dropwise condensation, biphilic (hydrophobic-hydrophilic) surface, size effect, partial flooding, heat transfer coefficient enhancement*

1. INTRODUCTION

The heat transfer coefficient for dropwise condensation (DWC) on vertical surfaces is an order of magnitude larger than that for filmwise condensation (FWC) (Glicksman and Hunt, 1972), however, the DWC is challenging to maintain and easily transits to FWC (Ghosh *et al.*, 2014). DWC consists of droplet nucleation, growth, coalescence, and departure followed by re-nucleation, with droplets ranging in size from the smallest nucleating droplets to departing droplets or even larger (Kim *et al.*, 2015). After the droplet reaches the departure size, sweeping occurs and this could accelerate the process of dropwise condensation since the falling droplet will coalesce with and sweep the droplets in its path (Dietza *et al.*, 2010). Under ideal dropwise condensation, the equilibrium size distribution for the droplets generally follows a power law distribution as incorporated in the so-called Rose model (Rose and Glicksman, 1972). In practice, various interfacial, constriction and other resistances can shift the droplet distribution, causing a reduction in the DWC heat transfer coefficient. To promote the DWC, micro/nano surface structures (Shang *et al.*, 2018 and Zarei *et al.*, 2018), as well as inorganic (gold) coatings Wilkins *et al.*, 1973, hydrophobic porous membranes (Hu and N. Chung, 2018) and hydrophobic organic (polymers (Lu *et al.*, 2015), self-assembled monolayers (Modak *et al.*, 2019)), wick structure in pipe (Yunus and S. Alsoufi, 2019) have been used. To further enhance the heat transfer coefficient, bilphilic (patterned hydrophobic and hydrophilic) surfaces have been created with one-dimensional (1-D) (Peng *et al.*, 2015) and two-dimensional (2-D) (Van Dyke *et al.*, 2015) patterns.

Due to the advantages of the DWC, its studies have a rather long history, including analytical studies of the dropwise condensation mechanism e.g., growth rate, drop size distribution, nucleation density. The direct simulations of the DWC also investigate the nucleation density, the effect of saturation temperature (Glicksman and Hunt, 1972), the drop size distribution (Leach *et al.*, 2016), the vapor pressure effect (Wu *et al.*, 2001), self-propelling mechanism for poly-sized droplets (Chen *et al.*, 2019). The DWC experiments generally are for surfaces larger than several hundred microns, the experimental evaluation of the

very small droplets is challenging (due to the rapid growth, large number of droplets, small scale, etc.). So far no study has addressed the surface size effect on enhancing the heat transfer coefficient of the DWC (and its direct simulations). Therefore, the surface size effect around and below hundred microns is addressed here with direct simulations using random droplet generation followed by the dropwise condensation processes. Then we consider periodic 1-D biphilic surface pattern, with the hydrophilic strips draining the condensate that formed in the hydrophobic strips by the DWC. We evaluate the surface-averaged heat transfer coefficient and compare with the available experimental results. The goal is to show the interplay of enhancement of the heat transfer by the surface size-effect of the hydrophobic domain, while avoiding flooding of the hydrophilic domain.

2. SIZE EFFECT OF DWC

When the domain size is below a threshold, as in biphilic patterned surfaces or partially-exposed surfaces, the droplets disappear at the boundaries. This intervening droplet removal process limits the maximum droplet size which in turn increases the heat transfer coefficient. Here we directly (numerically) simulate the DWC and evaluate the domain size effect and define the size-effect and no-size-effect regimes.

2.1 Direct simulation of DWC
Heat transfer through a droplet
Direct simulations of conduction through a droplet is made using the Star CCM+ code. The geometry is a spherical cap, as shown in Fig. 1(a). Progressively smaller mesh size was used until heat transfer results varied by less than 1%. The spherical cap can also be presented alternatively by a liquid film of uniform thickness δ_l (Modak *et al.*, 2019), through

$$\delta_l = \frac{k_l \Delta T_{sc}}{q},$$ (1)

---
* Corresponding author. Email: kaviany@umich.edu

where q is found from the direct simulation, k_l is the liquid thermal conductivity (0.68 W/m-K at 100°C for water), ΔT_{sc} is the subcooling between the solid surface and liquid-vapor interface (saturated condition) and 1 K is used in the simulations. The ratio of δ_l to droplet radius r_d is defined as

$$c_k = \delta_l / r_d. \tag{2}$$

The heat transfer coefficient (i.e., conductance per unit area) is

$$G/A = h = \frac{k_l}{\delta_l}. \tag{3}$$

The computed results for c_k as a function of contact angle θ_c are given in Fig. 1(b), e.g., for $\theta_c = 90°$, c_k is 0.109.

DWC dynamic simulations

The software MATLAB was used to simulate the DWC under random droplet nucleation, growth, coalescence (and re-nucleation) and departure (including merging at the boundaries).

The random droplet generation is implemented with the random generator in MATLAB to generate droplets in the target area and based on the droplet nucleation density.
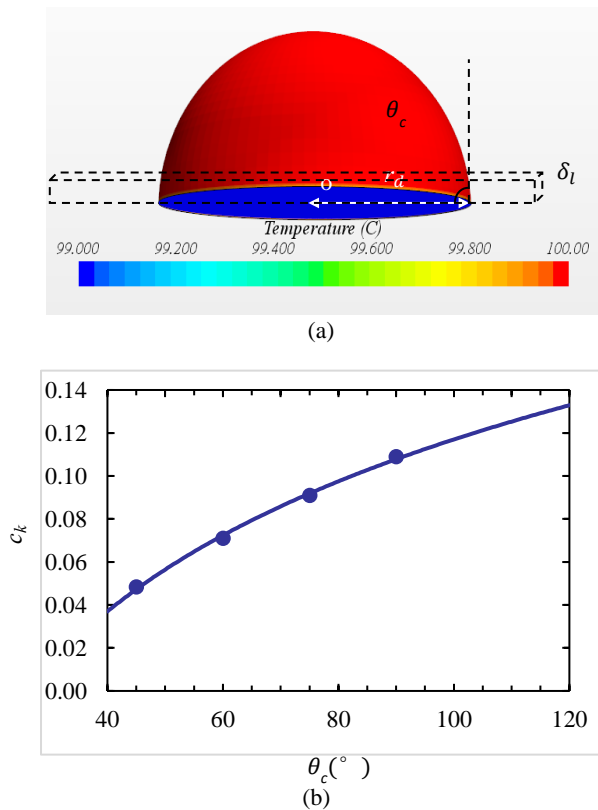

(a)

(b)

Fig. 1 (a) A snapshot of the simulated droplet temperature distribution with a contact angle of 90° using the Star CCM+ code. The corresponding uniform liquid film thickness is also shown. (b) Variations of the c_k with the contact angle θ_c.

The volume for spherical cap droplet is given as

$$V_d = \frac{\pi}{3} r_d^3 (2 + \cos\theta_c)(1 - \cos\theta_c)^2. \tag{4}$$

The droplet growth is by condensation of vapor on the droplet surface and by coalescence with neighboring droplets. The volumetric growth rate due to condensation is calculated from heat flow rate by

$$\dot{V}_d \rho_l \Delta h_{lg} = Q, \tag{5}$$

where ρ_l is the liquid density for water at 100°C (958 kg/m^3), Δh_{lg} is the heat of evaporation (2257 kJ/kg) and

$$Q = \sum \frac{k_l \Delta T_{sc}}{\delta_l} A_d = \sum \frac{k_l \Delta T_{sc}}{c_k r_d} \pi r_d^2 = \pi \frac{k_l \Delta T_{sc}}{c_k} \sum r_d, \tag{6}$$

$$\dot{V}_d = \pi \frac{k_l \Delta T_{sc}}{c_k \rho_l \Delta h_{lg}} \sum r_d. \tag{7}$$

At k^{th} timestep, the first-order time discretized form of Eq. (7) gives

$$V_{d_k} = V_{d_{k-1}} + \pi \frac{k_l \Delta T_{sc} r_d}{c_k \rho_l \Delta h_{lg}} \Delta t, \tag{8}$$

and using Eq. (4) we have

$$r_{d_k} = \left\{ V_{d_k} / \left[\pi (2 + \cos\theta_c)(1 - \cos\theta_c)^2/3 \right] \right\}^{1/3}. \tag{9}$$

The area-averaged heat flux $\langle q \rangle$ is

$$\langle q \rangle = \frac{Q}{L_z W_D}. \tag{10}$$

The thermal conductance $\langle G/A \rangle_D$ is

$$\langle G/A \rangle_D = \frac{\langle q \rangle}{\Delta T_{sc}}. \tag{11}$$

The heat flow rate for the dry surface (the surface that not covered by droplets) is negligible compared to the area covered by droplets. This is due to the very small thermal conductivity of the vapor compared to the liquid (in particular for water). Also, the radiation heat transfer from the vapor-covered surface is negligible because of the rather small subcooling common in the DWC. Due to the large nucleation density used here, the area fraction covered by droplets is also rather large. The neglecting of the heat transfer from the vapor-covered regions is also used in other direct simulations (Mikic, 1969). When two droplets touch (their center-center distance is less than the sum of their radii), a new droplet is created with the combined volume, and positioned at their center of mass. With coalescence, the combined droplet would be stored firstly, and the un-coalesced droplets would be updated at the end of each iteration. After coalescence, new droplets nucleate at the available exposed nucleation sites. Once the droplet reaches the departure radius (depending on substrate), it begins to slide along the assumed vertical surface in the direction of gravity. The sliding droplets will sweep all the droplets in their path until exiting the domain. The mechanisms of droplet departure and its speed are not addressed here, since for the optimal surface size effect, and in the case of the optimal biphilic surfaces, the droplets do not grow to be large enough to slip by gravity (even after coalescence). For larger surfaces the kinematics of the droplet departure should be addressed.

Other assumptions are: (i) before generating the random distribution for the droplets, the surface is assumed to be totally clean, (ii) all the droplets have the same initial radius $r_i = 0.5\,\mu$m (Leach *et al.*, 2016), (iii) when a droplet touches the domain boundary, it is deleted or merged (achieved by biphilic surface) and the droplet number is reduced by one, (iv) at every time step, there may be several coalescences called the subsidiary coalescence, so it is needed to ensure that there will be no more coalescences before the next time step, (v) the average of the last several steps are used for the final distribution, (vi) the vapor pressure remains constant during condensation at the saturation temperature, for water T_{lg} is 100°C, (vii) coalescence occurs instantaneously (Rose, 1966), (viii) contact angle θ_c is 90°, and (ix) there is no wall friction.

Sub-millimeter domain regime

The droplet nucleation density n_o is an important factor affecting the droplet number, droplet distribution, heat flux, etc. (Glicksman and Hunt, 1972). A submillimeter domain 40 μm × 100 μm, contact angle 90° and variable n_o are used to examine the predictions. With the increase in n_o, the droplet-size distribution becomes smoother, and the heat transfer coefficient rises. The droplet distributions for different n_o are shown in Fig. 2(a), (b) and (c). The blue lines are this study and the orange straight line is the Rose model (Rose and Glicksman, 1972), i.e.,

$$n_d(r_d) dr_d = \frac{1}{3\pi r_d^2 r_{max}} \left(\frac{r_d}{r_{max}} \right)^{-\frac{2}{3}} dr_d. \tag{12}$$
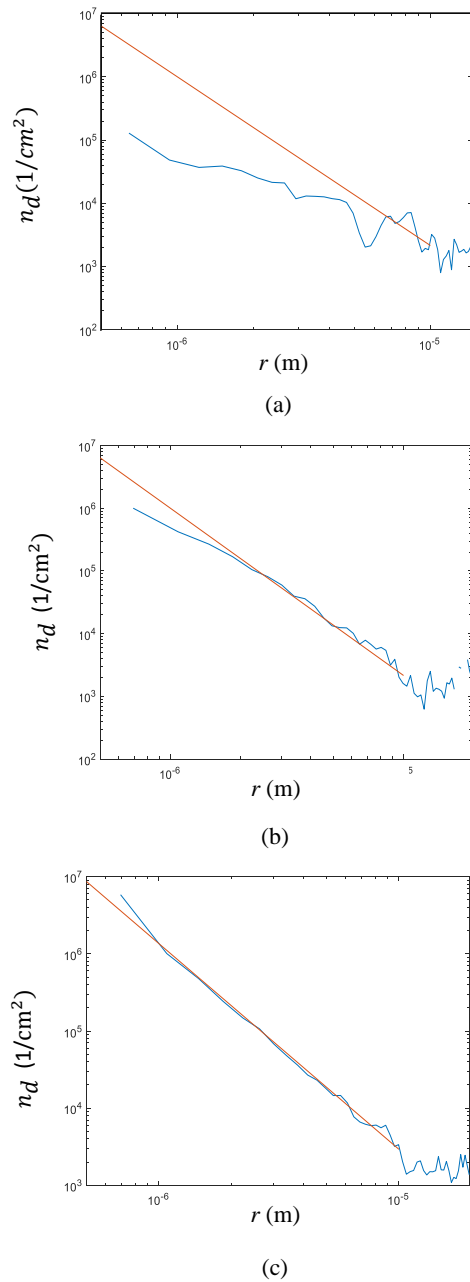
(a)

(b)

(c)

Fig. 2 Results of the droplet nucleation and growth simulation showing variations of the droplet-size number density distribution with respect to droplet radius for (a) $n_o = 10^6$, (b) 10^7 and (c) 10^8 1/cm^2.

For $n_o = 10^8$ 1/cm^2, the simulations are in agreement with the Rose distribution. For $n_o = 10^7$ 1/cm^2, the results diverge for droplet radius smaller than 2 μm, while for $n_o = 10^6$ 1/cm^2, this occurs for smaller than 7 μm. These results are similar to those reported in (Glicksman and Hunt, 1972). The difference between the results with time step of 10^{-6} and 10^{-5} s is within 2%, so 10^{-5} s is used.

As an example of sub-millimeter area, when the shorter dimension of the DWC surface (W_D) is 100 μm, then the largest droplet radius r_{max} is assumed to be 50 μm. However, the largest droplet is smaller than half the width as the simulation result shows in Fig. 3(a). This is because the largest droplet may touch the boundary and be deleted before it reaches the maximum. So, the maximum droplet radius r_{max} depends strongly on the domain size. The droplet nucleation density has a relatively small influence on the r_{max}. The results for $n_o = 10^6$ 1/cm^2 have some fluctuations.
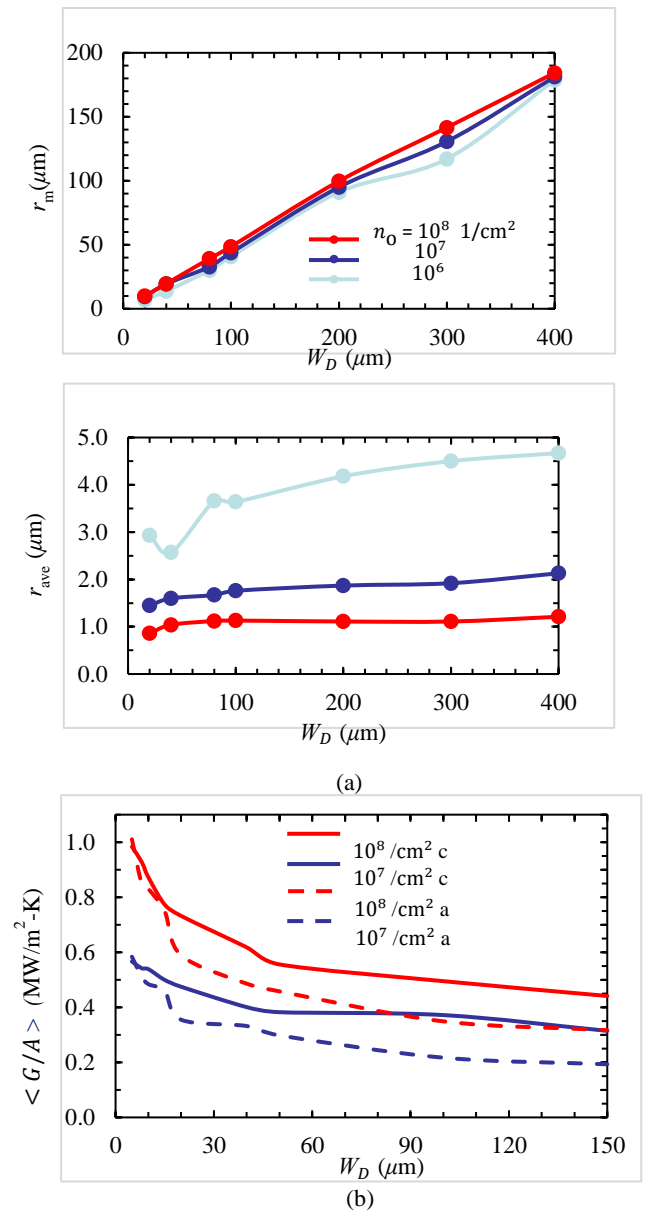

(a)

(b)

Fig. 3 (a) Variations of maximum and average droplet radius with respect to the domain width, for $n_o = 10^6$, 10^7 and 10^8 1/cm^2. (b) Comparison of the variations of the heat transfer coefficient using two different methods with respect to the domain width, for $n_o = 10^7$ and 10^8 1/cm^2.

For $n_o = 10^7$ and 10^8 1/cm^2, the average droplet radius r_{ave} is nearly independent of the width as shown in. 3(a), i.e., the droplet density is large enough to counter the influence of width increase. However, for $n_o = 10^6$ 1/cm^2, the r_{ave} grows a bit with the width. For $W_D = 400$ μm and $n_o = 10^6$ 1/cm^2, the large droplet is relatively small compared to the domain width, so it does not have high chance of touching the boundary, while the nucleation density is small. It also has a little chance of coalescing with other droplets, so the large droplet more likely stays in the domain, making r_{ave} relatively large compared to other n_o.

With the increase in W_D, the variations of the heat transfer coefficient (or G/A), for different n_o, are shown in Fig. 3(b). However, the extent of the deceasing trend is larger for the larger n_o. The results show that small W_D increases the heat transfer coefficient, since the average as well as the maximum droplet radius are small, so most of area is active and the small droplets can grow at high rate.

However, using the domain size to limit the r_{max} is not accurate as Fig. 3(a) showing the r_{max} always slightly smaller than half of W_D, a "cut

method" is proposed to simulate droplet with radius that exactly half the width we want. This is achieved by setting another domain large enough to accommodate several droplets with the maximum radius. Once the droplet reaches a preset maximum radius, it is forced to be deleted from the domain.

Compared with the heat transfer coefficient of the first method (shown with "a"), the heat transfer coefficient of the cut method (shown with "c") is higher, as shown in Fig. 3(b). This is because the former allows only for one droplet with the maximum radius and it is very unstable, the large droplets probably touch the boundary and disappear before reaching the maximum radius. With the cut method, it is certain that there are several droplets with the maximum radius, and the domain is large enough to accommodate them. Therefore, before they reach the maximum radius, they will continue to remain in the domain. With the decrease in W_D, the difference between the two methods becomes more pronounced. Since the cut method gives more accurate results, it will be used here.

Millimeter domain regime

The gravity sweeping occurs in DWC with millimeter-scale domain size. This is implemented with a sweeping mechanism by assuming that after a droplet reaches the departure size, it sweeps/shifts due to the gravity with a prescribed velocity 0.1m/s (Hassan, 2019). Small change about velocity will not affect the final result can be also verified. The sweeping droplets have higher chance of coalesce with other droplets within their tracts. A snapshot is also shown in Fig. 4.
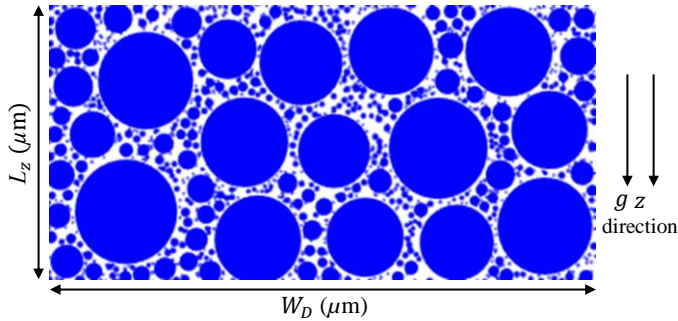

Fig. 4 Snapshot of the direct simulation of the DWC on a vertical surface. A video of the DWC dynamic simulation is available at this link site https://youtu.be/sYlTaBYhgxY. To create the video with reasonable computation, exaggerated small domain and corresponding scaled-down departing droplet radius are used.

To manage the extensive computation under very large droplet density starting with small initial radius of 0.5 μm, one method is ramping up the density, starting from 10^3 1/cm^2 and progressive increasing it after getting a converging result. However, beyond 10^6 1/cm^2 the computations are still extensive. Therefore, the "patch method" is proposed. This method predicts the results for high droplet nucleation density, by dividing the total simulation into two parts. One is the simulation for the large droplets starting with relatively large radius r_p (called patch radius), where the sweeping effect is included using the departure radius of 1 mm for copper substrate coated with gold (Lu, *et al*., 2015). The other is for the small droplets starting with the initial radius of 0.5 μm and ending with the r_p (using the cut method). The final result is the sum of two parts, i.e.,

$$G/A = X\,G_b/A + (1\text{-}X)\,G_s/A, \tag{13}$$

where X is the fraction of area covered by droplets with radius larger than r_p (Le Fevfie and Rose,1966), and X is

$$X = 1 - \left(r_p/r_{max}\right)^{1/3}. \tag{14}$$

The results are shown in Fig. 5. The patch radii used are from 15 to 100 μm, for $n_o = 10^7$ and 10^8 1/cm^2. In general, there is no patch radius

dependence (the difference is within 1%, which is negligible). It is because that as r_p increases, while the heat transfer coefficient of the small droplets and big droplets decrease, the fraction for small droplet increases (dominant). For large r_p, the simulation time for the large droplets is minimal for reaching the departure radius and sweeping effect, however, the simulation for the small droplets dominates the computation. The situations are reversed for small r_p. The $r_p = 40 \mu$m is used here for computing efficiency.
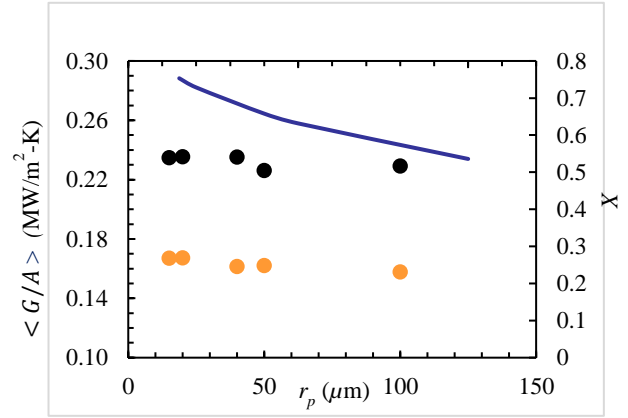

Fig. 5 Predicted variations of the thermal conductance per unit area for DWC and the fraction X, with respect to the patch radius. The results are for $n_o = 10^7$ (orange) and 10^8 1/cm^2 (black). The blue curve is for the X.

Filmwise condensation

As W_D increases, flooding occurs in the lower portion of the condenser, i.e., the DWC will turn into filmwise condensation (FWC). The Nusselt integral analysis of the filmwise condensation on vertical surface is (Carey, 1992)

$$G/A = 0.943\left(\tfrac{k_l}{L_z}\right)\left[\tfrac{\rho_l(\rho_l-\rho_g)g\Delta h_{lg}L_z^3}{k_l\mu_l\Delta T_{sc}}\right]^{1/4}. \tag{15}$$

It is assumed that the flow of condensate remains laminar ($\rho_g = 0.597$ kg/m^3, $g = 9.8$ m/s^2, $\Delta h_{lg} = 2257$ kJ/kg, $k_l = 0.679$ W/m-K, and $\mu_l = 2.78\times10^{-4}$ N-s/m^2). For subcooling of $\Delta T_{sc} = 1$ K and $L_z = 200$ mm, this give $G/A = 0.0174$ MW/m^2-K, which is about ten times smaller than the DWC.

2.2 Size-Effect Regime Diagram

The cut and patch methods discussed above are used to simulate DWC with gold-coated copper substrate of variable domain size W_D ($L_z = W_D$) from micrometer to meter. The conditions are: $\theta_c = 90°$, droplet departure radius of 1 mm (Lu *et al*., 2015), liquid-vapor interfacial conductance $(G/A)_{lg} = 5\times10^6$ MW/m^2-K, and the constriction resistance of 20% of the total resistance which is significant for the large droplets (Carey, 1992).

The results for the heat transfer coefficient as a function of the domain size (although using the cut method, the x axis here is two times of the maximum radius) are shown in Fig. 6. There are three regimes, namely, the DWC size-effect regime, the DWC no size-effect regime (with gravity sweeping), and the FWC regime. From the FWC to no size-effect regime, there is an enhancement by ten folds, while from the no size-effect to the size effect regime, there is another ten folds enhancement. The band between $n_o = 10^7$ and 10^8 1/cm^2 is marked as extra enhancement although achieving $n_o = 10^8$ 1/cm^2 is rather challenging in experiments.

The results of the existing simulations (Rose, 2002) and experiments (Alwazzan *et al*., 2017, Hoenig, and Bonner, 2018, O'Neill, and Westwater, 1984) are also shown in Fig. 6, with good agreement with the predictions of this study. The result for condensation of a 1-D biphilic

surface tube is adjusted for the fraction of the DWC area and only half of that area (top surface) is assumed to be not flooded. The minimum W_D (1μm) which gives the maximum heat transfer coefficient is limited by a single droplet nucleation when there is only one droplet in the domain. So far, there are no experiments for $W_D < 100\ \mu$m, so the comparison between simulations and experiments has not been extended there either.
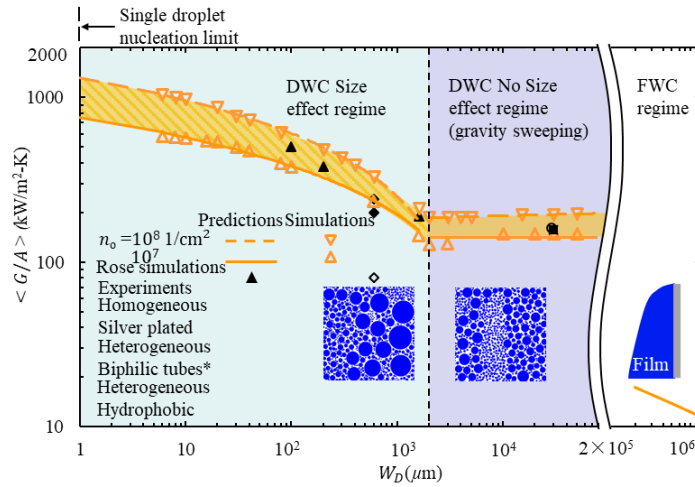

Fig. 6 The DWC size effect regime diagram showing the variations of the heat transfer coefficient with respect to the width of the hydrophobic surface. The simulation snapshots for different regimes, the experimental results and the calculated results for FWC are also shown.

3. SIZE EFFECT in 1-D BIPHILIC SURFACE

As the condenser length increases, the departing droplets accumulated downstream create flooding and then DWC will transition to FWC which reduces the heat transfer coefficient. What's more, the high heat transfer coefficient from size effect is based on assumption that droplets will merge at the boundaries of W_D. But this is ideal and not achievable for only hydrophobic surface in reality. To remedy this, the 1-D biphilic surface consisting of alternating hydrophobic and hydrophilic strips can help drain the condensate from hydrophobic strips into the neighboring hydrophilic strips which allow for downward flow of the liquid as isolated rivulets. This was realized in the experiment reported in (Peng et al., 2015). Here the Computational Fluid dynamics (CFD) simulations of this 1-D biphilic surface is conducted for the optimal combination of the hydrophilic strip width (W_F) and hydrophobic strip width (W_D) for different condenser length (L_z) and subcooling (ΔT_{sc}).

3.1 Direct Simulation of Liquid Rivulet

Geometry

The schematic of the circular 1-D biphilic surface used in the experiments of (Peng et al., 2015) is shown in Fig. 7(a). It is made of unit cells of two different strips. The contact angles for hydrophobic surface and hydrophilic surface is 90° and 60° respectively, to match those experiments. The hydrophilic strips are considered as liquid rivulets which are assumed to have a cylindrical cap cross section formed by the surface tension. So, the maximum pressure drop along the rivulet is limited by the critical pressure across this liquid-vapor interface http://www.insula.com.au/physics/1279/L8.html. This gives

$$\Delta p_c = \frac{\sigma}{r} = \frac{2\sigma \sin\theta_c}{W_F}, \tag{16}$$

where σ is the surface tension for water at 100 °C, $\sigma = 0.059$ N/m, r is the radius of cylinder.
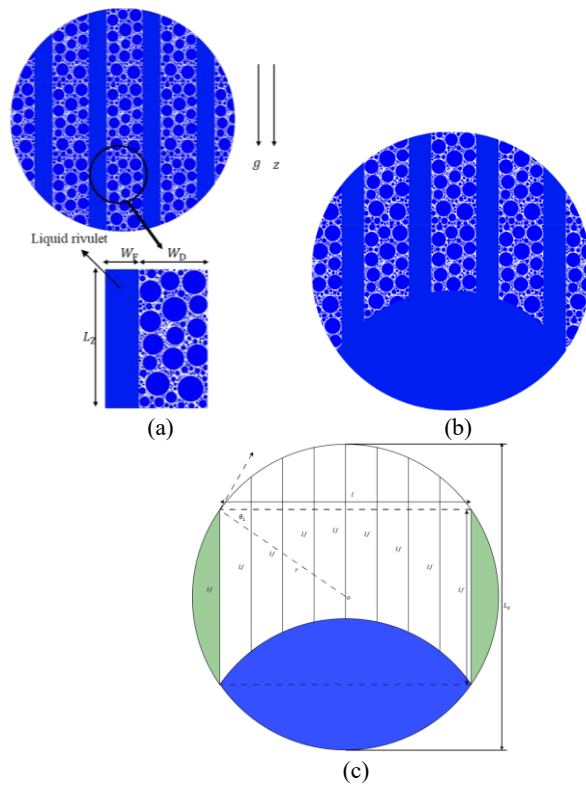

(a)

(b)

(c)

Fig. 7 Schematic of the circular 1-D biphilic surface (Peng et al., 2015), with the unit-cell strip widths and the condenser length. (b) A rendering of the hydrophilic rivulet flooding at a distance L_f from the top, results in the partial flooding of the lower part of the condenser. (c) Details in geometry plot of the flooded lower region and its geometric parameters.

Flooding

The condensate formed within W_D is drained along the z direction (along the gravity vector) in this liquid rivulet. If rivulet viscous pressure drop Δp that getting from the CFD simulation is larger than Δp_c, there is flooding downstream along L_z. A location is marked as L_f which is defined as critical length (where $\Delta p = \Delta p_c$). For $L_z > L_f$, it is assumed that the surface floods so that region below becomes ineffective area with negligible heat transfer, as shown in Fig. 7(b). The geometric relation for the 1-D biphilic circular surface and the related parameters are shown in Fig. 7(c). The blue segment is flooded area and the rest is effective area. The radius r is the half of the total length L_z. The parameters l and θ_1 shown in Fig. 7(c) are calculated by

$$l = 2[r^2 - (\tfrac{L_f}{2})^2]^{0.5}, \tag{17}$$

$$\theta_1 = \arccos\left(\frac{0.5l}{r}\right). \tag{18}$$

The areas of the white-marked region "wh" and the green region "gr" in the Fig. 7(c) are

$$A_{wh} = L_f l, \tag{19}$$

$$A_{gr} = 2A_{arch} = 2\left(\pi r^2 \frac{2\theta_1}{2\pi} - 0.5 L_f 0.5l\right) = 2(r^2\theta_1 - 0.25 L_f l). \tag{20}$$

The total effective area is the sum of white and green parts,

$$A_e = A_{wh} + A_{gr} = L_f l - 2(r^2\theta_1 - 0.25 L_f l). \tag{21}$$

The DWC width fraction is

$$\alpha_1 = \frac{W_D}{W_D + W_F}. \tag{22}$$

The area fraction for effective area with partial flooding is

$$\alpha_2 = \frac{A_e}{A} = \frac{L_f l - 2(r^2\theta_1 - 0.25 L_f l)}{\pi r^2}. \tag{23}$$

The heat flux for the 1-D biphilic surface under partial flooding is

$$q = <G/A>_D \Delta T_{sc} \alpha_1 \alpha_2, \tag{24}$$

where $<G/A>_D$ is thermal conductance from Fig. 6 with size effect of DWC and $n_o = 10^7$ $1/cm^2$.

The thermal conductance for the 1-D biphilic surface is

$$<G/A> = <G/A>_D \alpha_1 \alpha_2. \tag{25}$$

The total heat flow rate is

$$Q_D = <G/A>_D \Delta T_{sc} W_D L_z = Q_F = \dot{m} \Delta h_{lg} W_F L_z. \tag{26}$$

The mass flux is given by

$$\dot{m} = \frac{W_D}{W_F} \frac{<G/A>_D \Delta T_{sc}}{\Delta h_{lg}}. \tag{27}$$

The Star CCM+ code is used for the calculation of the rivulet viscous flow under gravity. Typical predicted pressure drop profile, pressure distribution along the rivulet with the marking of the critical pressure drop (which indicates flooding beyond this distance L_f) and the liquid velocity vector field are shown in Figs. 8(a), (b) and Fig. 9. Fig. 8 and Fig. 9 are all for $W_F = 400$ μm and $L_z = 25$ mm. The initial condition for the liquid rivulet simulation is $p = 0$ Pa; $u_x = 0$ m/s, $u_y = 0$ m/s, $u_z = 0$ m/s. The boundary condition are: (i) the top curved surface is wall type (slip surface with zero shear stress), (ii) the bottom surface is mass flow inlet type (no slip with specific mass flux given), (iii) the outlet surface is constant pressure outlet type ($p = 0$ Pa), and (iv) the inlet arch surface is wall type (no slip surface).

In Figs. 8(a), (b), the liquid flows along the direction of gravity (z direction) and the total pressure drop is 482 Pa. The maximum pressure appears at the entrance, and the minimum pressure is 0 Pa set at the end. The maximum velocity is at the outlet, which is 0.233 m/s. A close-up of the liquid velocity vector field within the rivulet near the exit region is also shown in Fig. 9.

To compare the predictions of the W_D size effect and flooding in W_F, the experimental conditions (Peng et al., 2015) of $W_D = 950$ μm, and variable W_F are imposed. The pressure drop within W_F as a function of W_F with circular condenser of diameter L_z are shown in Fig. 10(a) and for subcooling of 2, 4, and 6 K. The corresponding critical pressure drop for the given W_D is also marked.
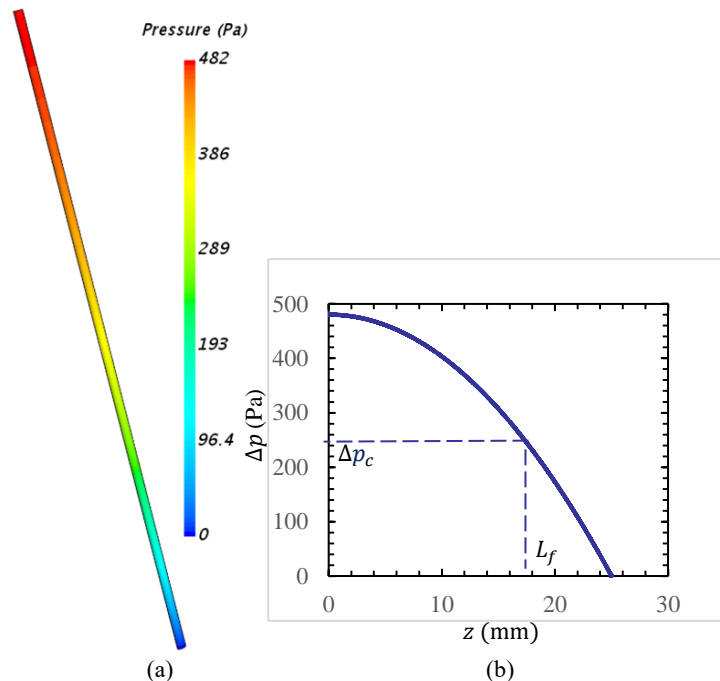

Fig. 8 (a) Predicted pressure profile along the liquid rivulet flowing down the hydrophilic strip (b) Pressure distribution along the rivulet with respect to distance from origin in z direction.
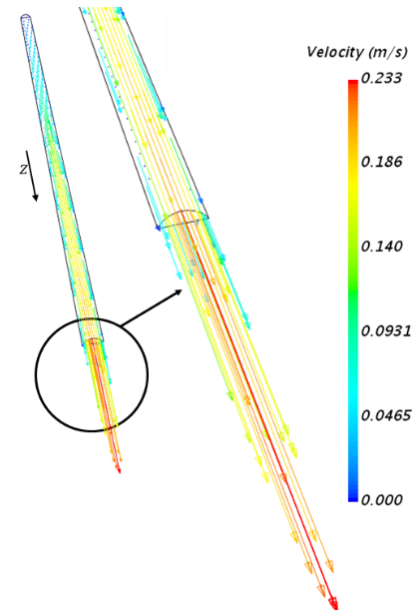

Fig. 9 Predicted liquid velocity vector field within the rivulet and the close-up near the exit region. The results are all for $W_F = 400$ μm and $L_z = 25$ mm.

With increase in W_F, the rivulet pressure drop decreases, which is duo to viscosity, the critical pressure drop also decreases but not as much as viscous pressure drop. Therefore, the intersections indicate the point that flooding starts.

Figure 10(b) shows the variations of the flooding length L_f with respect to W_F, for three different subcooling. These are the x axis value for intersection points between the critical pressure horizontal line and the curve in Fig. 8(b). And there is a critical hydrophilic strip width $W_{F,c}$ where $\Delta p = \Delta p_c (L_z = L_f)$. For $L_z > L_f$, the downstream of the L_f will flood as rendered in Figs. 7(b) and (c). With the decrease in W_F, L_f decreases. With a larger subcooling, L_f decreases since the condensate mass flux entering W_F increases.

From the above results, the variations of the $W_{F,c}$ with respect to the W_D is shown in Fig. 11. Showing that for given W_D, there is an optimal combination of two strip widths for subcooling of 0.1, 0.5, 1, 2, 4, and 6 K. The larger the subcooling, the larger is $W_{F,c}$. With a decrease in W_D, the $W_{F,c}$ also decreases. However, the drop is not as pronounced as that in the W_D. As W_D tends to zero, all results tend to converge to zero.

3.2 Results and Comparison with Experiment

From Fig. 10(b) and Eqs. (17)-(27), the results for variations of the surface averaged heat flux and heat transfer coefficient with respect to the W_F are shown in Figs. 12(a) and (b), for three subcooling and given W_D and L_z, for the circular condenser of Fig. 7(a). The area-averaged heat flux first increases with W_F due to an increased condensate draining capacity and then decreases owing to a smaller area fraction (occupied by the DWC strip) available for heat transfer. The predictions are in good agreement with the experimental results of (Peng et al., 2015). The shaded region indicates partial flooding when the W_F is smaller than the $W_{F,c}$, which are 495, 634, and 738 μm for subcooling of 2, 4, and 6 K respectively. The dashed line indicates the ideal heat flux under no flooding (extremely small subcooling). The average heat flux is proportional to the subcooling, while the average heat transfer coefficient is independent of subcooling when there is no flooding. Upon flooding, the heat transfer coefficient suffers depending on subcooling.

Figures 12(c) and (d) show similar variations, but with respect to the W_D while W_F is constant. With increase in the W_D, the heat flux increases, reaching a maximum and then decreases. So, for a given W_F the hydrophobic strip cannot be too small (not enough heat transfer area) or
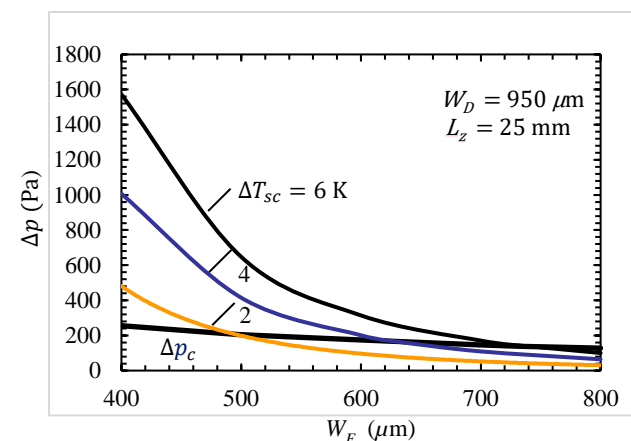
(a)
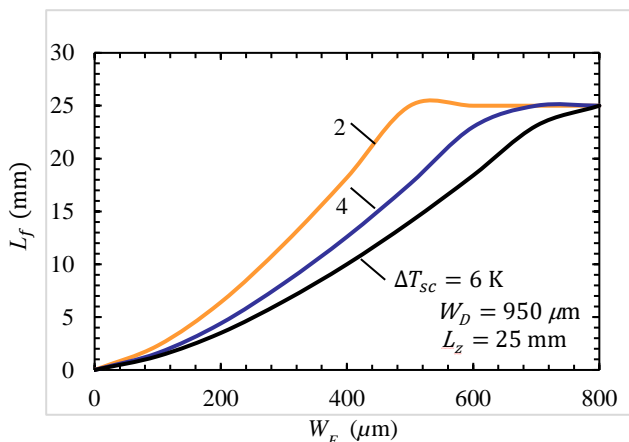
(b)

Fig. 10 (a) Variations of the rivulet pressure drop with respect to the hydrophilic strip width of the 1-D biphilic surface, for subcooling of 2, 4, and 6 K. The variation of the capillary pressure with respect to the hydrophilic strip width is also shown. (b) The variations of the flooding length with respect to the hydrophilic strip width, for subcooling of 2, 4, and 6 K.
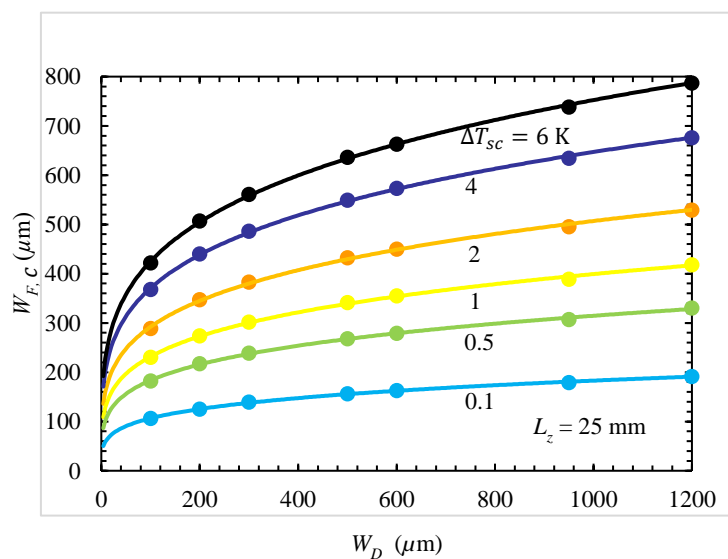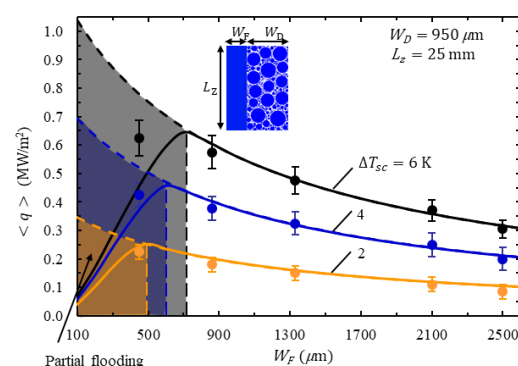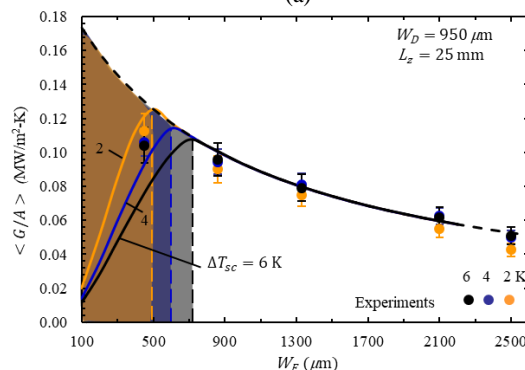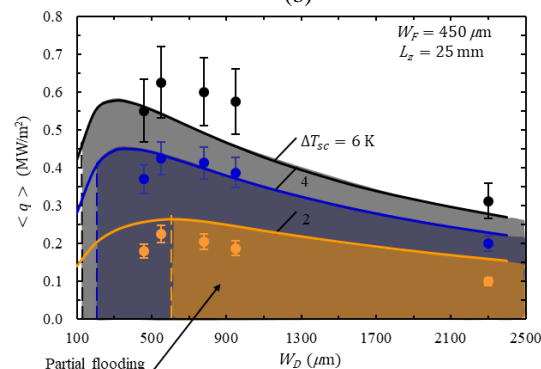

Fig. 11 Variations of the critical hydrophilic strip width (i.e., when flooding starts to occur) with respect to the hydrophobic strip width, for subcooling of 0.1, 0.5, 1, 2, 4, and 6 K.
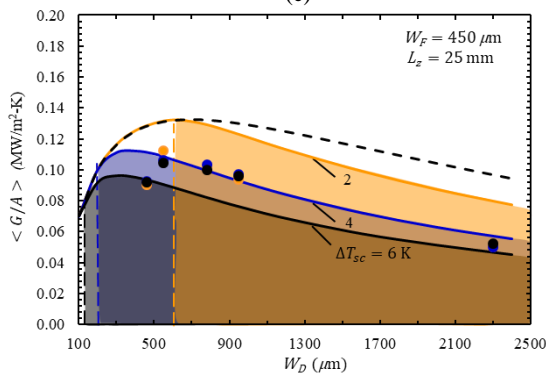

(a)

(b)

(c)

(d)

Fig. 12 Variations of the predicted (a) heat flux and (b) heat transfer coefficient with respect to the hydrophilic strip width (for hydrophobic strip width of 950 μm); Variation of the predicted (c) heat flux and (d) heat transfer coefficient with respect to the hydrophobic strip width (for hydrophilic strip width of 450 μm) for different subcooling, and comparison with the experimental results. The regimes of partially flooding are marked with shades. For (d) the predicted limiting case of zero subcooling is also shown with broken lines.

too large (flooding in W_F). The predicted results are still in good agreements with the experimental results which have large scatter (Peng *et al.*, 2015). The deviation might result from the assumptions like the flooded region for this study, depicted in Fig. 7(b) and the difference of contact angles compared to experiments and so on. The shaded areas mark flooding occurring at $W_D = 600$, 218, and 127 μm for subcooling of 2, 4, and 6 K, respectively. The dashed line in Fig. 12(d) implies no flooding (diminishing subcooling).

3.3 Optimized size effects for 1-D biphilic surface

To demonstrate the optimal performance, we choose a subcooling of 2 K, and examine the variations of the average heat transfer coefficient with respect to the W_F for several W_D from 100 to 5000 μm, as shown in Fig. 13. The end points for all the lines are the onset of flooding given by Fig. 11. The loci of the end points to all curves on the top left portion of the figure representing the maximum heat transfer coefficient are marked by the red dashed line. There are two regimes, the biphilic size effect regime, and the biphilic no size effect regime, and these are consistent with the results of Fig. 6 (for the DWC domain only). The two regimes are separated by the hydrophobic strip width of 2000 μm. The dotted line shows the upper limit for the hydrophobic surface only, the hydrophobic strip width is in the range of 2 mm and 200 mm (no size effect DWC). The marked point on the left axis is the experimental result for the hydrophobic surface only (23% below the maximum measured 1-D biphilic surface results in (Peng *et al.*, 2015)). The marked point on the top of the right axis is the predicted maximum for a biphilic surface with W_D of 200 mm.

We compare three sets of experimental results (Peng *et al.*, 2015) with our predictions. The hollow orange symbols represent the predictions while the filled symbols represent the experiments. The hollow and filled squares overlap, so, for $W_F = 930$ μm and $W_D = 2100$ μm, implying a very close match between prediction and experiment. For $W_F = 450$ μm and $W_D = 550$ μm combination, the prediction is about 16% higher. For the combination $W_F = 2100$ μm and $W_D = 2500$ μm, the difference is rather large and this can be due to the extent flooding occurs along the hydrophobic strip which is not accounted for in our model, so flooding in the biphilic no size effect regime with large W_F and W_D needs closer examination.

Since the 1-D biphilic surface enhances DWC in the size effect regime, the variation of the maximum heat transfer coefficient with respect to the W_F for W_D from 100 to 1200 μm and subcooling of 0.1, 0.5, 1, 2, 4, and 6 K is shown in Fig. 14. With decrease of the W_D, the optimal W_F (which is $W_{F,c}$) also decreases, the overall heat transfer coefficient increases, reaching a peak (optimal) and then decreases. The optimal $W_{F,c}$, W_D pairs are marked for each subcooling.

With the decrease in subcooling, smaller W_D (which follows smaller $W_{F,c}$) can be used and the size effect shows in the enhanced average heat transfer coefficient. The optimal $W_{F,c}$, W_D pair become smaller as the subcooling decreases. The broken line connects the loci of the optimal pairs giving the maximum average heat transfer coefficient for different subcooling values. For subcooling < 0.1 K, the maximum average heat transfer coefficient increases to a high value, although such a small subcooling 0.1 K is difficult to achieve in practice. The optimal $W_{F,c}$, W_D for 2 K in experiment (Peng *et al.*, 2015) is 450, 550 μm while the result from our model is 435, 528 μm which is really close.

Fig. 14 Variations of the predicted maximum (optimal) heat transfer coefficient with respect to the hydrophilic stripe width, for various subcooling. For each subcooling the effect of variation in the hydrophobic strip width is also shown, along with the values for the peak performance (broken line). The above results were for a circular condenser to compare with the experiments.

To generalize the results, a 1-D rectangular biphilic surface is also considered. The variations of the maximum average heat transfer coefficient with respect to condenser length L_z for subcooling of 0.1, 0.5, 1, 2, 4, and 6 K are shown in Fig. 15(a), (b) for W_D of 950 and 600 μm respectively. For different subcooling, the maximum heat transfer coefficient starts at different point for a constant length. With the decrease of L_z, the maximum heat transfer coefficient increases. In the limit of $L_z \rightarrow 0$, all the lines tend to converge to the predicted heat transfer coefficient for a single hydrophobic surface by dropwise condensation simulation. The dashed line shows when subcooling is small enough, the heat transfer coefficient becomes independent of the condenser length. For different W_D, the trends remain the same while the maximum heat transfer coefficient for diminishing length rises for smaller W_D due to the size effect in Fig. 6. Figure 15 could directly show this.

4. SUMMARY AND CONCLUSIONS

The hydrophobic vertical surfaces cause dropwise condensation allowing for higher heat transfer coefficient (or specific conductance G/A) compared to filmwise condensation on hydrophilic surfaces. The 1-D biphilic surfaces made of periodic hydrophobic and hydrophilic strips allow for efficient draining of the condensate generated from the W_D through the W_F and can further enhance surface averaged G/A, i.e., $<G/A>$. In addition, for small W_D, the droplets adjacent to the W_F merge with the draining liquid rivulet there before reaching their maximum departing radii and this causes enhancement in the G/A within W_D (called size effect of DWC). Also noting that the G/A within W_F is negligible due to the rather thick flowing liquid rivulet there. Additionally, the rivulet can become unstable and cause flooding when the condensate flow rate reaches a critical value. This threshold is reached when the viscous pressure drop along the rivulet (along the direction for gravity) reaches
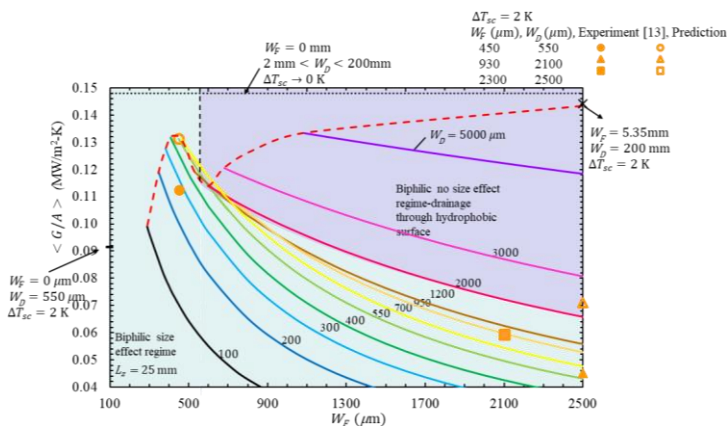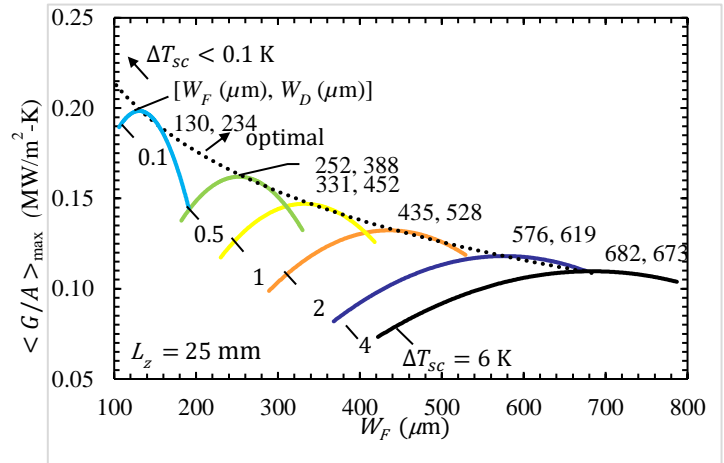

Fig. 13 Variations of the predicted average heat transfer coefficient with respect to the hydrophilic strip width, for a subcooling of 2 K and different hydrophobic strip widths. Two regimes are identified as size effect (enhancement occurs), and no size effect regimes (W_D itself could generate flooding and decrease $<G/A>$ obviously but is not shown here).

the capillary pressure within it. The viscous pressure drop depends on the mass flux and the geometry of liquid rivulet while the capillary pressure is determined by the contact angle θ_c and W_F. Then the 1-D biphilic surface can be optimized to maximize the size effect of W_D while keeping W_F to a minimum and avoiding flooding.
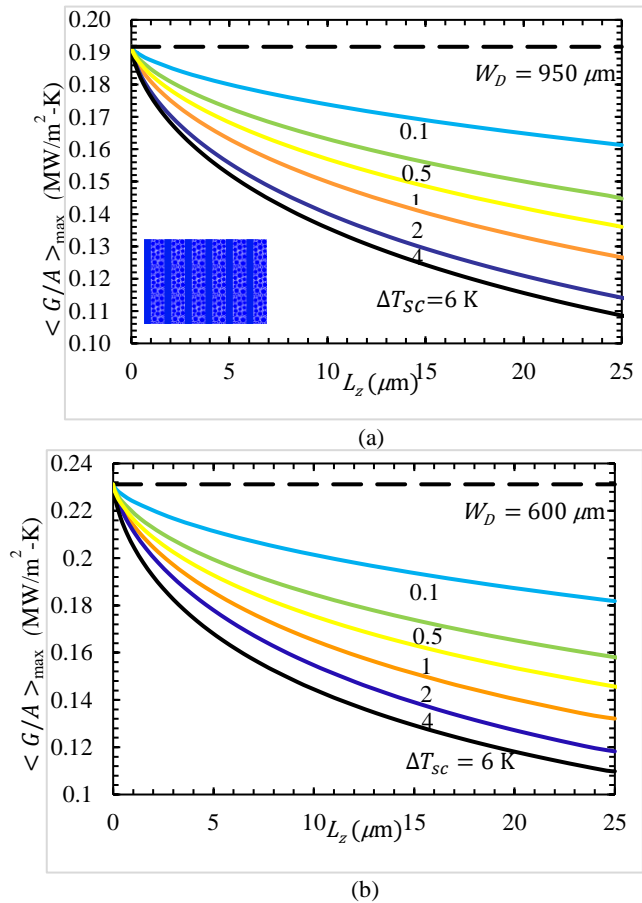

Fig. 15 Variations of the maximum heat transfer coefficient with respect to the condenser length, for several subcooling. (a) $W_D = 950$, and (b) $600\ \mu$m. The results are for a 1-D rectangular biphilic surface.

Here through direct simulations of the droplet nucleation, growth, coalescence, merging at the boundaries of W_D, re-nucleation and departure and through the direct simulations of the rivulet condensate flow and pressure drop within W_F, the area average $<G/A>$ for the total 1-D biphilic surface is predicted for condensation and contact angles of $90°$ and $60°$ for W_D and W_F are used respectively. The results are summarized below.

(i) Figure 4 shows a snapshot for direct DWC simulation and the video of the droplet nucleation, growth, coalescence, merging at the boundaries of W_D, re-nucleation and departure is also available.

(ii) The predicted homogeneous hydrophobic surface size effect is shown in Fig. 6, where the size effect begins when W_D is smaller than 2 mm and the G/A increases smoothly till the physical limit of the nucleation site diameter is reached. The results for the lower droplet nucleation density of $10^7\ 1/cm^2$ rather better match the experimental results, so this is chosen for the rest of the analysis.

(iii) To compare the predicted results with the available experimental results of (Peng *et al*., 2015), their circular condenser surface and similar conditions are used and shown in Fig. 7, and it is assumed that once the rivulets flood in W_F, the entire surface below the flooding length L_f is covered with the condensate and heat transfer for this ineffective area is negligible. The simulated rivulet profile and the predicted L_f for specific geometry are shown in Fig. 8 and Fig. 9. The effect of subcooling on the critical flooding width and length is shown in

Fig. 10. The corresponding minimum W_F for no flooding, i.e., $W_{F,c}$ is shown in Fig. 11.

(iv) The predicted size effects (enhancement in W_D and flooding in W_F) on the $<G/A>$ under experimental conditions of (Peng *et al*., 2015) are shown in Fig. 12, and it is shown that under large subcooling the flooding is more pronounced and there are optimal W_D and W_F values for each subcooling. There are good agreements with the experimental results.

(v) Beyond the conditions of the experiments (Peng *et al*., 2015), the results are generalized for very small ($\Delta T_{sc} \rightarrow 0$) and moderate subcooling, and variable condenser length (a 1-D rectangular biphilic condenser) including very small values (tending to zero). For $\Delta T_{sc} = 2$ K, the optimal W_D and W_F values are found and two regimes (the size effect regime where W_D is below 2 mm and the no size effect regime.) are identified which is consistent with Fig. 6 for homogeneous hydrophobic surface. In Fig. 13, we also show that the optimal $<G/A>$ has an upper bound which is for ($\Delta T_{sc} \rightarrow 0$) with $W_F = 0$ (i.e., homogeneous hydrophobic surface).

(vi) We also show the effect of ΔT_{sc} on the optimal W_D and $W_{F,c}$ values in Fig. 14, which shows $<G/A>_{max}$ decreasing monotonically with increase in ΔT_{sc} for the optimal pairs of W_D and $W_{F,c}$. Finally, similar monotonic decrease is shown with increasing condenser length in Fig. 15.

The predicted results show that for moderate ΔT_{sc} and condenser length ranges, optimal W_D and W_F values give similar enhanced $<G/A>$ results reported in several experiments. Therefore, with a proper combination of the W_F, the W_D, the L_z and ΔT_{sc}, we can get a better enhancement of overall heat transfer coefficient in 1-D biphilic surface.

NOMENCLATURE

A	area (m^2)
AR	specific thermal resistance [K/(W/m^2)]
c_k	film-thickness to droplet-radius ratio
D	distance between two droplets (m)
g	gravity (m/s^2)
G	Conductance (W/K)
h	heat transfer coefficient [W/(m^2-K)]
Δh_{lg}	heat of vaporization (J/kg)
k	thermal conductivity (W/m-K)
L	length (m)
$\dot{m}$	mass flux (kg/m^2-s)
n_o	droplet nucleation density (1/cm^2)
n_d	number of droplets
p	pressure (Pa)
Δp	pressure drop (Pa)
q	heat flux (W/m^2)
Q	heat flow rate (W)
r	radius (m)
t	time (s)
T	temperature (ºC or K)
ΔT	temperature difference (ºC or K)
u	velocity (m/s)
V	volume (m^3)
W	width (m)
X	droplet coverage fraction
x, y, z	coordinate (m)

Greek Symbols

α	area fraction
δ	film thickness (m)
ρ	density (kg/m^3)
θ_c	contact angle (°)
μ	viscosity (N-s/ m^2)
σ	surface tension (N/m)

Subscripts

b	big droplet
c	critical value
con	constriction
d	droplet
D	dropwise condensation
f	flooding
F	filmwise condensation
g	gas or vapor
i	initial condition
inter	interfacial
l	liquid
lg	liquid-vapor saturation
max	maximum
p	patch method
s	small droplet
sc	subcooling

others

< >	area averaged

REFERENCES

Alwazzan, M., Egab, K., Peng, B., Khan, J., and Li, C., 2017, "Condensation on hybrid-patterned copper tubes (I): Characterization of condensation heat transfer," *International Journal of Heat and Mass Transfer*, **112**, 991-1004.
https://dx.doi.org/10.1016/j.ijheatmasstransfer.2017.05.039

Barati, S.B., Pinoli, J.-C., Gavet, Y., and Valette, S., 2017, "Differential and average approaches to Rose and Mei dropwise condensation models," *International Journal of Mathematical Models and Methods in Applied Sciences*, **11**, 40-46.

Bostwick, J., and Steen, P., 2018, "Static rivulet instabilities: Varicose and sinuous modes," *Journal of Fluid Mechanics*, **837**, 819-838.
https://dx.doi.org/10.1017/jfm.2017.876

Carey, V.P., 1992, *Liquid-vapor Phase-Change Phenomena*, Hemisphere Publishing Corporation.

Chen, X., Lu, J., and Tryggvason, G., 2019, "Numerical simulation of self-propelled non-equal sized droplets," *Physics of Fluids*, **31**, 052107
https://dx.doi.org/10.1063/1.5094757

Dietza, C., Rykaczewski, K., Fedorov, A. G., and Joshi, Y., 2010, "Visualization of droplet departure on a superhydrophobic surface and implications to heat transfer enhancement during dropwise condensation, " *Applied Physics Letters*, **97**, 033104.
https://dx.doi.org/10.1063/1.3460275

Ghosh, A., Beaini, S., Zhang, B. J., Ganguly, R., and M. Megaridis, C., 2014, "Enhancing Dropwise Condensation through Bioinspired Wettability Patterning", *Langmuir*, **30**(43), 13103-13115.
https://dx.doi.org/10.1021/la5028866

Glicksman, L.R., and Hunt JR, A.W., 1972, "Numerical simulation of dropwise condensation," *International Journal of Heat and Mass Transfer*, **15**, 2251-2269.
https://dx.doi.org/10.1016/0017-9310(72)90046-4

Hassan, G., Yilbas, B., Al-Sharafi, A. and Al-Qahtani, H., 2019, "self-cleaning of a hydrophobic surface by a rolling water droplet," *Scientific Reports*, **9**, 5744.
https://dx.doi.org/10.1038/s41598-019-42318-3

Hoenig, S.H., and Bonner, R.W., 2018, "Dropwise Condensation on Superhydrophobic Microporous Wick Structures," *Journal of Heat Transfer*, **140**, 071501-1.
https://dx.doi.org/10.1115/1.4038854

Hu, H., and N. Chung, J., 2018, "A molecular dynamics simulation of nanoscale water vapor absorption on the surface of LiBr aqueous solution," *Frontiers in Heat and Mass Transfer*, **11**, 24.
https://dx.doi.org/10.5098/hmt.11.24

Kim, M.-K., Cha, H., Birbarah, P., Chavan, S., Zhong, C., Xu, Y., and Miljkovic, N., 2015, "Enhanced Jumping-Droplet Departure," *Langmuir*, **31**(49), 13452-13466
https://dx.doi.org/10.1021/acs.langmuir.5b03778

Leach, R.N., Stevens, F., Langford, S.C., and Dickinson, J.T., 2006, "Dropwise Condensation: Experiments and Simulations of Nucleation and Growth of Water Drops in a Cooling System," *Langmuir*, **22**(21), 8864–8872.
https://dx.doi.org/10.1021/la061901+

Le Fevfie, E.J., and Rose, J.W., 1966, "A theory of heat transfer by dropwise condensation," Proc. Third Int. Heat Transfer Conference, Am. Inst. Chem. Engrs. New York 2,362.

Lu, C.-H., Beckmann, M., Unz, S., Gloess, D., Frach, P., Holst, E., Lasagni, A., and Bieda, M., 2015, "Heat transfer model of dropwise condensation and experimental validation for surface with coating and groove at low pressure", *International Journal of Heat and Mass Transfer*, **52**(1), 113–126.
https://dx.doi.org/10.1007/s00231-015-1641-0

Mikic, B., 1969, "On mechanism of dropwise condensation," *International Journal of Heat and Mass Transfer*, **12**(10), 1311–1323.
https://dx.doi.org/10.1016/0017-9310(69)90174-4

Modak, S., Kaviany, M., Hoeing, S.H., and Bonner, R.W., 2019, "Numerical analysis of meniscus dynamics in monolayer-wick dropwise condensation," J. *Numerical Heat Transfer*, **76**(5), 301–322.
https://dx.doi.org/10.1080/10407782.2019.1627829

O'Neill, G. A., and Westwater, J.W., 1984, "Dropwise condensation of steam on electroplated silver surfaces," *International Journal of Heat and Mass Transfer*, **27**(9), 1539-1549.
https://dx.doi.org/10.1016/0017-9310(84)90266-7

Peng, B., Ma, X., Lan, Z., Xu, W., and Wen, R., 2015, "Experimental investigation on steam condensation heat transfer enhancement with vertically patterned hydrophobic–hydrophilic hybrid surfaces," *International Journal of Heat and Mass Transfer*, **83**, 27–38.
https://dx.doi.org/10.1016/j.ijheatmasstransfer.2014.11.069

Rose, J.W., 1966, "On the mechanism of dropwise," *International Journal of Heat and Mass Transfer*, **10**, 755-762.
https://dx.doi.org/10.1016/0017-9310(67)90135-4

Rose, J.W., 2002, "Dropwise condensation theory and experiment: a review", *Proceedings of the Institution of Mechanical Engineers, Part A: Journal of Power and Energy*, **216**(2), 115–128.
https://dx.doi.org/10.1243/09576500260049034

Rose, J.W. and Glicksman, L.R., 1972, "Dropwise condensation-The distribution of drop sizes," *International Journal of Heat and Mass Transfer*, **16**, 411-425.
https://dx.doi.org/10.1016/0017-9310(73)90068-9

Shang, Y., Hou, Y., Yu, M., and Yao, S., 2018, "Modeling and optimization of condensation heat transfer at biphilic interface," *International Journal of Heat and Mass Transfer* ,122, 117–127. https://dx.doi.org/10.1016/j.ijheatmasstransfer.2018.01.108

Tsuruta, T., and Tanaka, H., 1991, "A theoretical study on the constriction resistance in dropwise condensation," *International Journal of Heat and Mass Transfer*, **34**(11), 2779-2786. https://dx.doi.org/10.1016/0017-9310(91)90237-9

Van Dyke, A.S., Collard, D., M Derby, M., and Rachel Betz, A., 2015, "Droplet coalescence and freezing on hydrophilic, hydrophobic, and biphilic surfaces," *Applied Physics Letters*, **107**, 141602. https://dx.doi.org/10.1063/1.4932050

Wilkins, D. G., Bromley, L. A. and Read, S. M., 1973, "Dropwise and filmwise condensation of water vapor on gold,"
AIChE Journal, 19(1), 119-123.
https://dx.doi.org/10.1002/aic.690190117

Wu, Y., Yang, C., Yuan, X., 2001, "Drop distributions and numerical simulation of dropwise condensation heat transfer," *International Journal of Heat and Mass Transfer*, **44**(23), 4455-4464. https://dx.doi.org/10.1016/S0017-9310(01)00085-0

Yunus, M., and S. Alsoufi, M., 2019, "Development of a heat pipe and grey based Taguchi method for multi-output optimization to improve thermal performance using hybrid nanofluids," *Frontiers in Heat and Mass Transfer*, **12**, 11. https://dx.doi.org/10.5098/hmt.12.11

Zarei, S., Talesh Bahrami, H.R., and Saffari, H., 2018, "Effects of geometry and dimension of micro/nano-structures on the heat transfer in dropwise condensation: A theoretical study," *Applied Thermal Engineering*, **137**, 440-450. https://dx.doi.org/10.1016/j.applthermaleng.2018.04.003